Tellus (2002), 54A, 63–75
Printed in UK. All rights reserved

TELLUS
ISSN 0280–6495

Nonhydrostatic aspects of coastal upwelling meanders and filaments off eastern ocean boundaries

By SHENN-YU CHAO[1] and PING-TUNG SHAW[2], [1]*Horn Point Laboratory, University of Maryland Center for Environmental Science, Cambridge, Maryland 21613-0775, USA;* [2]*Department of Marine, Earth and Atmospheric Sciences, North Carolina State University, Raleigh, North Carolina 27695-8208, USA*

(Manuscript received 13 June 2000; in final form 12 June 2001)

ABSTRACT

Coastal upwelling meanders and filaments are common features off eastern ocean boundaries. Their growth is reinvestigated herein using a nonhydrostatic three-dimensional model and a reduced-gravity model, with the objective of assessing contributions from two mechanisms that emerge in the nonhydrostatic regime. The first mechanism is caused by the vertical projection of the Coriolis force in the momentum equation. It is found that the vertical Coriolis force often acts as a restoring force against numerical damping off eastern ocean boundaries and thus enhances the growth of meanders and filaments. The second mechanism arises from unstable ocean stratification when the cold upwelled water intrudes seaward over the warm layer. The unstable stratification, albeit transient, further enhances the growth of meanders and filaments. It is concluded that although nonhydrostatic effects do not change our understanding of how meanders and filaments grow, the realism can be enhanced using a nonhydrostatic model insofar as meanders and filaments off eastern ocean boundaries are concerned.

1. Introduction

Meanders and eddies along a coastal upwelling front are common features off eastern ocean boundaries (Brink, 1987; Narimousa and Maxworthy, 1989). Under persistent upwelling-favorable winds, cold upwelled water in the near-shore region intrudes seaward, producing a series of meanders and eddies. In extreme cases, a few meanders manage to outgrow adjacent ones and intrude seaward as filaments of varying width, strength, and seaward excursion distance. Figure 1 illustrates schematically the three-dimensional structure of a large-amplitude meander (or a cold filament) off the eastern ocean boundary. Large-amplitude meanders are normally confined to the upper 100–200 m of the coastal ocean. Off the California coast, filaments in their fully developed stage can extend 200–300 km offshore. They are typically 20–50 km wide and are separated by a meridional distance of 100–150 km (Flament et al., 1985). Temperature can be 2–3 °C lower inside a filament than in the surrounding water. In a particularly well developed filament, seaward current speeds can be as large as 50–100 cm s^{-1} (Davis, 1985; Kosro and Huyer, 1986).

The California coastal ocean is not the only example; similar features also exist off the west coast of Spain. Røed and Shi (1999) provided an extensive review of these observed features. Cold filaments off Spain are about 30–50 km wide (Haynes et al., 1993; Sousa, 1995). Their seaward excursion ranges up to 250–300 km. The separation distance between filaments is about 80 km but can be as large as 150 km. Typically, filaments occur at preferred locations and seem to be related to capes and submarine ridges.

* Corresponding author.
e-mail: pt_shaw@ncsu.edu

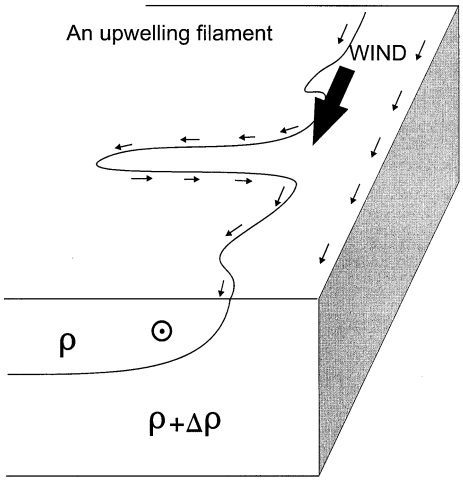

Fig. 1. A three-dimensional illustration of an upwelling filament off the eastern ocean boundary. Thick and thin arrows illustrate wind direction and the surface ocean current, respectively. Filaments vary in strength and size; this schematic pattern is suggestive of a strong filament, in which the circulation is much stronger than the wind-induced Ekman drift. If a filament is weak, the landward current associated with the filament can be offset by the seaward Ekman drift.

In terms of numerical modeling, dynamic processes leading to the development of large-amplitude meanders and cold filaments have been examined by McCreary et al. (1991), Haidvogel et al. (1991), Batteen (1997), and Røed and Shi (1999). The hydrostatic approximation is assumed in these models. Vertical resolution ranges from one active layer to ten levels. All these models identify filaments as relatively inviscid features. In order to enhance the growth of filaments, the horizontal viscosity and mixing must be minimized by either increasing horizontal model resolution or reducing mixing coefficients. Two length scales point to the need for high resolution. The wavelengths of typical growing instabilities responsible for meanders and eddies are from 10 to 30 km (Fukamachi et al., 1995; Røed and Shi, 1999; Shi and Røed, 1999). The typical internal Rossby radius is 10 km. The horizontal resolution is 5.5 km in McCreary et al. (1991), from 2.8 to 21.1 km in Haidvogel et al. (1991), and about 10 km in Batteen (1997). In this range of horizontal resolution, the use of biharmonic mixing rather than the conventional Laplacian mixing was found necessary to suppress small-scale mixing to enhance the growth of filaments; biharmonic mixing is an imperfect alternative to encourage filament growth at coarse resolutions. The 2-km resolution used in Røed and Shi (1999) resolves the length scales relevant to filaments, and sizable filaments are produced without the use of biharmonic mixing.

The effect of planetary (β-) dispersion appears to enhance the growth of large-amplitude meanders. The β-dispersion was included in McCreary et al. (1991), Batteen (1997), and Røed and Shi (1999). Among these models, Batteen (1997) contrasts solutions with and without planetary dispersion. Without the β-dispersion, the westward excursion of filaments is either reduced or completely eliminated. The β-dispersion must be one of the reasons why eddies, meanders and filaments become so pronounced near eastern ocean boundaries. The model of Haidvogel et al. (1991) did not include β-dispersion and wind forcing. In that limit, the growth of filaments is induced by coastline irregularities, as demonstrated by Batteen (1997). It should be noted that the β-enhancement of meanders and filaments is a slow process; the southward water movement gradually attains cyclonic vorticity, which leads to formation of eddies. By comparison, the frontal instability is a much stronger mechanism requiring no β-dispersion. Thus, with the frontal instability fully accounted for, high-resolution models, such as Røed and Shi (1999), can produce filaments without β-dispersion.

A continental slope is included in the models of Haidvogel et al. (1991) and Batteen (1997) and in Røed and Shi (1999), to a certain extent. Its effect is succinctly explained by a linear stability analysis of Shi and Røed (1999). A meandering upwelling front contains two types of unstable waves. The first type is associated with the frontal instability (frontal mode), and the second type is induced by a mixed barotropic–baroclinic instability (mixed mode). The linear stability analysis of Shi and Røed (1999) reveals that a bottom slope reduces the growth rate of the frontal mode slightly without changing its phase speed. For the mixed mode, the phase speed is only slightly reduced. Thus, the effect of a variable bottom topography on unstable waves appears to be marginal.

These earlier papers demonstrate the growth of meanders and filaments off eastern ocean boundaries in hydrostatic models. At the present time,

it is not clear whether a nonhydrostatic model is necessary to produce realistic meanders, noting that the skill of hydrostatic models is still progressing rapidly with finer resolution. Nevertheless, we feel that it is of interest to investigate how mechanisms in the nonhydrostatic regime contribute to the meander growth. The balance at issue is in the vertical momentum equation. Let u, v and w be the eastward, northward, and vertically upward velocity components, respectively. The vertical momentum balance is

$$\frac{Dw}{Dt} - (2\Omega \cos\phi)u = -\frac{1}{\rho_0}\frac{\partial p}{\partial z} - \frac{g\rho}{\rho_0} + \text{mixing} \qquad (1)$$

where $D/Dt = \partial/\partial t + u\partial/\partial x + v\partial/\partial y + w\partial/\partial z$ is the substantial differential operator, $\Omega = 2\pi\ \mathrm{d}^{-1}$ is the earth's rotational frequency, ϕ is the latitude, and ρ is the perturbation density about a reference seawater density $\rho_0 = 1025\ \mathrm{kg\ m^{-3}}$. Other notations are conventional. The hydrostatic approximation ignores vertical acceleration, Coriolis deflection, and mixing in eq. (1). In hydrostatic models, the computation is stable if vertical acceleration is small. For oceanic processes that do not involve large vertical acceleration, nonhydrostatic effects can be safely neglected. Problems involving large vertical acceleration, however, are outside the realm of hydrostatic models, which do not treat the nonhydrostatic effect properly. One major source of vertical acceleration is unstable ocean stratification that triggers vertical convection. Hydrostatic models parameterize unstable stratification by either using an instantaneous convective adjustment scheme, such as in the Bryan–Cox general circulation model (Bryan, 1969), or increasing vertical diffusion of density drastically, such as in the Princeton Ocean Model (Mellor, 1993).

Vertical acceleration may become considerably larger in nonhydrostatic models than in hydrostatic models. In the present subject, two mechanisms in eq. (1) contribute to strong vertical motions. The Coriolis acceleration produces downwelling motion for seaward (westward) surface currents and upwelling motion for landward (eastward) surface currents. The expectation from linear models is that downwelling motion induces cyclonic vorticity while upwelling generates anticyclonic vorticity in the upper ocean. Beyond the Coriolis acceleration, unstable ocean stratification also induces strong vertical acceleration. As illustrated in Fig. 1, the seaward excursion of cold water over the warm layer provokes unstable stratification whose effect can be examined only in the nonhydrostatic regime.

A nonhydrostatic regional model is formulated in Section 2 to study meanders and filaments along a coastal upwelling front off an eastern ocean boundary. Major results from the nonhydrostatic model are summarized in Section 3. The growth rate of meanders and filaments off an eastern ocean boundary could be generally increased by including the vertical component of the Coriolis force. Moreover, occasional unstable stratification could further enhance this process. Intuitively, it is not clear how the vertical Coriolis acceleration induces the meander growth. A heuristic reduced-gravity model is formulated in Section 4 as a diagnostic tool to examine this issue.

2. Three-dimensional nonhydrostatic model formulation

The formulation of the nonhydrostatic model essentially follows the procedure outlined in the paper by Williams (1969) with a few modifications. Under the Boussinesq approximation, the three-dimensional momentum, continuity and density equations are

$$\frac{D\boldsymbol{v}}{Dt} + 2\Omega\boldsymbol{k}' \times \boldsymbol{v} = -\frac{1}{\rho_0}\nabla p - \frac{\rho g}{\rho_0}\boldsymbol{k} - A_4\nabla_H^4\boldsymbol{v} + \nu\frac{\partial^2\boldsymbol{v}}{\partial z^2} + Y\boldsymbol{j} \qquad (2)$$

$$\nabla\cdot\boldsymbol{v} = 0 \qquad (3)$$

$$\frac{D\rho}{Dt} = -K_4\nabla_H^4\rho + \kappa\frac{\partial^2\rho}{\partial z^2} \qquad (4)$$

where $\boldsymbol{v}$ is the three-dimensional velocity vector, $\boldsymbol{j}$ is a northward unit vector, $\boldsymbol{k}'$ is a unit vector pointing upward from the North Pole, and $\boldsymbol{k}$ is the local upward unit vector. The subscript H changes the gradient operator from three-dimensional to horizontal. The β-effect is retained to enhance filament growth, and ϕ is 40°N, the center latitude of the domain. Following McCreary et al. (1991) and Batteen (1997), horizontal mixing coefficients are biharmonic with $A_4 = 3\times10^9\ \mathrm{m^4\ s^{-1}}$ and $K_4 = 3\times10^8\ \mathrm{m^4\ s^{-1}}$ to provoke filament growth. For vertical diffusion, the

commonly used turbulence closure schemes such as Mellor and Yamada (1974) have not been finely tuned to fit a nonhydrostatic model. For this reason, vertical viscosity and diffusivity are chosen to be constant with $\nu = \kappa = 0.2\ \mathrm{cm^2\ s^{-1}}$. Since ν and κ are small, downward transfer of wind-induced shear stress is hindered. Consequently, the equatorward wind forcing is projected into the upper ocean as a body force

$$Y = \frac{\tau_0}{\rho_0 d\sqrt{\pi}} \exp\left(-\frac{z^2}{d^2}\right) \tag{5}$$

where $\tau_0 = -1\ \mathrm{dyn\ cm^{-2}}$ and $d = 60$ m. The scaling factors in eq. (5) ensure that the depth-integrated body force is equivalent to a wind stress of $1\ \mathrm{dyn\ cm^{-2}}$ at the sea surface. The treatment of wind forcing as a body force is quite common in models with low friction (see, for example, Gill and Clarke, 1974).

The horizontal domain is 210 km by 210 km and bounded to the east by a straight coastline. The horizontal and vertical resolutions are 3 km and 20 m, respectively. The sea surface is capped by a free-slip, impermeable, rigid lid to filter out surface gravity waves. Since the wind stress is included in eq. (2), no additional stress is needed at the sea surface. The downward vertical extent of the ocean is truncated by placing a free-slip and insulating bottom at $z = -H$, where $H =$ 400 m. Coastal upwelling meanders and filaments are mostly trapped in the upper ocean with a weak barotropic flow component extending to the bottom. A shallow ocean bottom or the presence of bottom stress normally enhances the barotropic flow component slightly (McCreary and Chao, 1985). By placing the free-slip bottom at 400 m depth, the barotropic flow component is not visibly enhanced, and the stress-free bottom reduces the accumulation of the barotropic component. In several preliminary experiments, the maximum ocean depth was increased twofold or fourfold by compromising vertical resolution. Results were not visibly different near the ocean surface, justifying the choice of a 400 m ocean depth.

The initial front and the meridional jet are parallel to the coastline and in geostrophic balance. The initial velocity and perturbation density profiles are similar to those used in Kielmann and Käse (1987), Chao (1994), and Shi and Chao (1995):

$$\rho = \frac{-\Delta\rho}{2\cosh^2(z/D)}\left[\mathrm{erf}\left(\frac{x - x_0}{l}\right) - 1\right] \tag{6}$$

$$v = \frac{-gD\,\Delta\rho}{\sqrt{\pi}\rho_0 l f} \exp\left(\frac{-(x - x_0)^2}{l^2}\right) \times \left(\tanh\frac{z}{D} + \tanh\frac{H}{D}\right) \tag{7}$$

where $\Delta\rho = 1\ \mathrm{kg\ m^{-3}}$, $D = 100$ m, $l = 10$ km, $x_0 = -20$ km, and erf is the error function. Figure 2 shows a zonal section of the initial perturbation density field (thin lines) and alongshore velocity (thick lines).

The horizontal boundary conditions are as follows. The coastal wall is free-slip and impermeable. The north, south and west boundaries are open; normal gradients of all dependent variables, including the normal flow component, are zero. At these open boundaries, values outside the open boundary are set to values at the adjacent grid just inside the boundary at every time step of numerical integration. Since all horizontal mixing terms are biharmonic, each lateral boundary condition must be paired with a higher-order boundary condition to make the problem well posed. Let $B\alpha = 0$ be a boundary condition in which B is the boundary operator and α a dependent

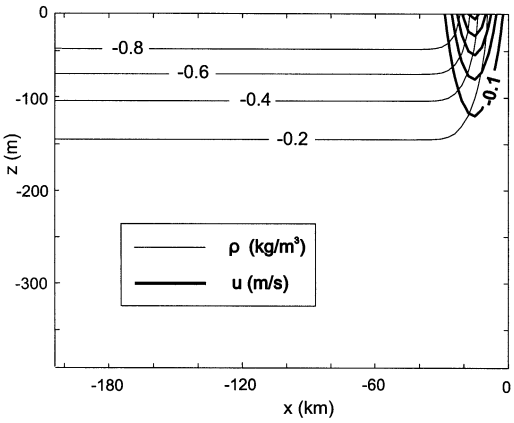

Fig. 2. A zonal section of the initial distribution of isopycnals and the equatorward jet used in the nonhydrostatic model. The initial geostrophic frontal jet is uniform in the alongshore direction. The contour interval for the alongshore velocity is $0.1\ \mathrm{m\ s^{-1}}$. The perturbation density (ρ) is in units of $\mathrm{kg\ m^{-3}}$.

variable. The standard choice takes $\nabla_H^2 B\alpha = 0$ as an additional constraint.

An open boundary with the above zero-gradient condition is often misinterpreted as a highly reflective boundary because the boundary condition is no-flux. On the contrary, the boundary condition often results in over-transmitting in terms of the Courant–Friedrich–Lewy (CFL) criterion because momentum and density are transmitted over one grid spacing in one time step. In other words, the "sluice gate" is opened to allow for somewhat unrestricted inflow or outflow of density and momentum across the open boundary. Enlarging the horizontal domain to reduce the boundary effect in several preliminary numerical experiments indicates that the zero-gradient condition does not affect the model results insofar as the nonhydrostatic contributions to meanders and filaments are concerned.

Perhaps the biggest difference between hydrostatic and nonhydrostatic models is how the pressure field is computed. Taking the divergence of eq. (2), time derivatives become zero as required by flow continuity (3). Thus, the pressure field is governed by the three-dimensional Poisson equation, which is solved by the preconditioned conjugate gradient (PCG) method (e.g., Pozrikidis, 1997). Once the pressure field is determined, velocity and density fields are calculated through time stepping. In this model, integration in time is done by using the Adams–Bashforth scheme as in Marshall et al. (1997). An occasional Euler step is used to smooth the integration. The grid system is Arakawa-C, and spatial derivatives are center-differenced to second-order accuracy.

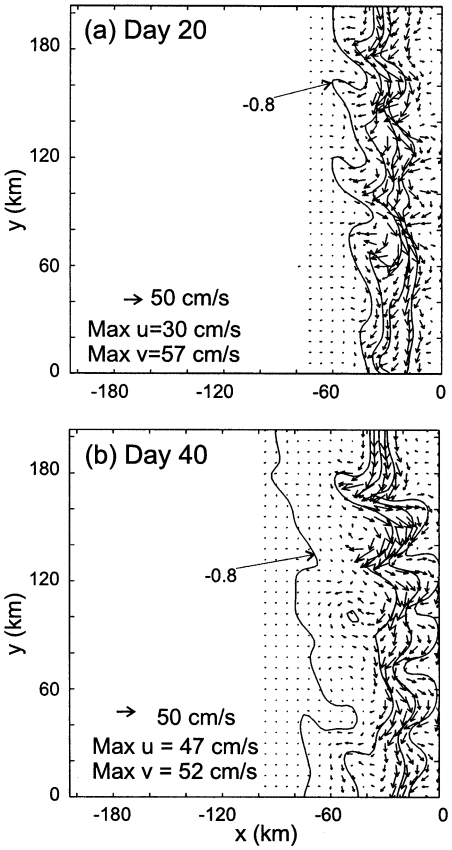

Fig. 3. Surface flow and the perturbation density field for the all-inclusive nonhydrostatic experiment at (a) day 20 and (b) day 40. Perturbation density contours start from $-0.8\ \mathrm{kg\,m^{-3}}$ for the outermost contour and increase landward at an interval of $0.2\ \mathrm{kg\,m^{-3}}$.

3. Nonhydrostatic numerical results

Figure 3 shows the surface flow and perturbation density fields at days 20 and 40. Being forced by a constant equatorward wind stress, the initially shore-parallel front evolves into a series of wavenumber-four meanders, and isopycnals migrate seaward in response to wind forcing. Our preliminary analysis (not presented here) indicates that nonhydrostatic contributions are quite small up to day 40. While instability theories such as Fukamachi et al. (1995) may give clues to the meander wavelength, the subsequent growth to large-amplitude meanders is made possible by the equatorward wind forcing (Batteen, 1997).

Figure 4 shows surface features at days 60, 80 and 100. From day 60 to 80, a particularly well developed anticyclonic eddy centered at $y =$ 140 km forms between two meander crests. Subsequently, a filament develops on the equator side of the eddy. By day 100, the filament, as defined by the $-0.6\ \mathrm{kg\,m^{-3}}$ perturbation density contour, has grown to a size of 80 km long and 20 km wide. Currents are strong in the meanders and eddies nearshore but become exceedingly weak farther out to the sea. At day 100, for example, the seaward current associated with the offshore filament protruding around $y = 96$ km is

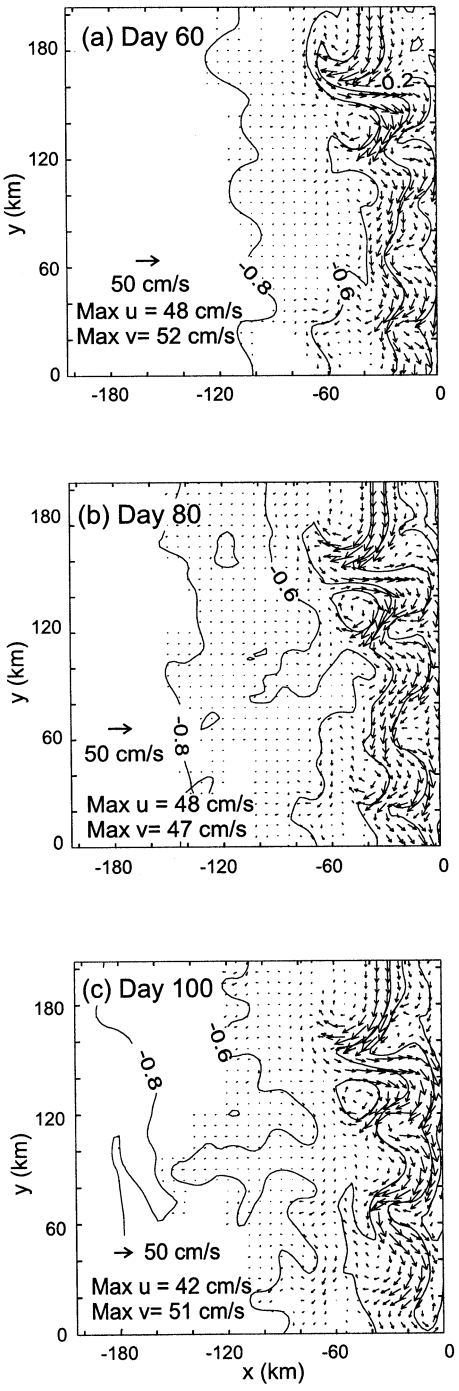

Fig. 4. Same as Fig. 3 but (a) day 60, (b) day 80, and (c) day 100. The contour interval for the perturbation density is 0.2 kg m^{-3}.

barely visible in Fig. 4(c). Inside the filament, a slightly stronger seaward surface current than the surrounding westward Ekman drift propels the seaward intrusion.

Figure 5 shows contours of perturbation density (thin lines) and alongshore velocity (thick solid and dashed lines) at day 100 in a zonal section located at $y = 96$ km, approximately through the axis of the filament. Several features are noteworthy. First, the stratification in the upper 80 m of the ocean between $x = -140$ and -60 km is slightly unstable underneath the nose of the seaward intruding filament, as indicated by the -0.6 kg m^{-3} density contour. Downward convection beneath the dense plume apparently homogenizes most of the unstable stratification. Second, a sizable poleward undercurrent (dashed thick lines) with speeds up to 10 cm s^{-1} develops beneath the equatorward jet, which hugs the coast (solid thick lines). The undercurrent is continuous in the alongshore direction, more or less following the meandering equatorward jet above. Under equatorward wind forcing, an undercurrent may be produced by the alongshore variation of wind speed, a meandering front, bottom topography, or the coastal orientation (McCreary, 1981; McCreary et al., 1991; Batteen, 1997). In the present rectangular basin under uniform wind

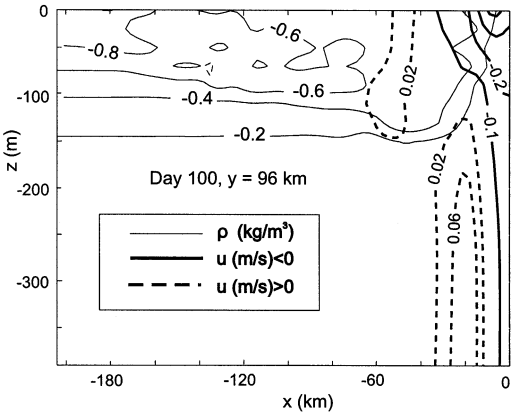

Fig. 5. A zonal section of perturbation density (thin lines) and alongshore currents (thick lines) at day 100 from the all-inclusive nonhydrostatic solution. The section is taken at $y = 96$ km, approximately slicing though the axis of the long filament in Fig. 4(c). Contour intervals are 0.2 kg m^{-3} for perturbation density, 0.1 m s^{-1} for the southward velocity (solid lines), and 0.04 m s^{-1} for the northward velocity (dashed lines).

forcing, alongshore variability arises solely from the meandering front. It is not surprising that the undercurrent develops below the frontal zone. Figure 6 shows a three-dimensional perspective of the filament at day 100. The perturbation density surface $\rho = -0.6$ kg m^{-3} is chosen for this illustration. The nose of the seaward intruding filament is shallow. Behind the nose, the filament deepens to a depth of 80 m or so. As illustrated in Fig. 5, stratification in the rear portion of the filament ranges from neutral to slightly unstable because of continuous downward convection.

Figure 7 illustrates distributions of vertical velocity (w) at 50 m depth and normalized relative vorticity (ζ/f) at 30 m depth at day 100. The offshore and nearshore thick contour lines are surface isopycnals with $\rho = -0.6$ and -0.4 kg m^{-3}, respectively. Shading indicates downwelling speeds in excess of 0.01 cm s^{-1} in the top panel and anticyclonic vorticity in excess of $0.2f$ in the bottom panel. The distribution in the upper ocean is generally coherent vertically in this case, and choices of the particular depths are mainly to reduce patchiness. The distribution of vertical velocity presents a significant departure from hydrostatic expectations. Following the isopycnal surface with $\rho = -0.4$ kg m^{-3} southward, downwelling (upwelling) occurs beneath the seaward (landward) arm of a meander. While this result is consistent with expectations from the vertical momentum balance in the nonhydrostatic regime [eq. (1)], a hydrostatic model would normally produce the opposite result. Vertical flow speeds generally decrease with distance away from the coast. The distribution of relative vorticity also concentrates in the coastal area and is mostly 90° out of phase with the distribution of the vertical speed. Cyclonic vorticity is concentrated about meander crests, while anticyclonic vorticity is mostly centered in troughs.

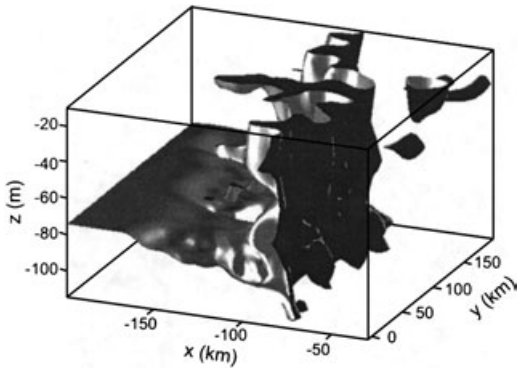

Fig. 6. A three-dimensional illustration of the -0.6 kg m^{-3} perturbation density surface at day 100 from the all-inclusive nonhydrostatic solution.

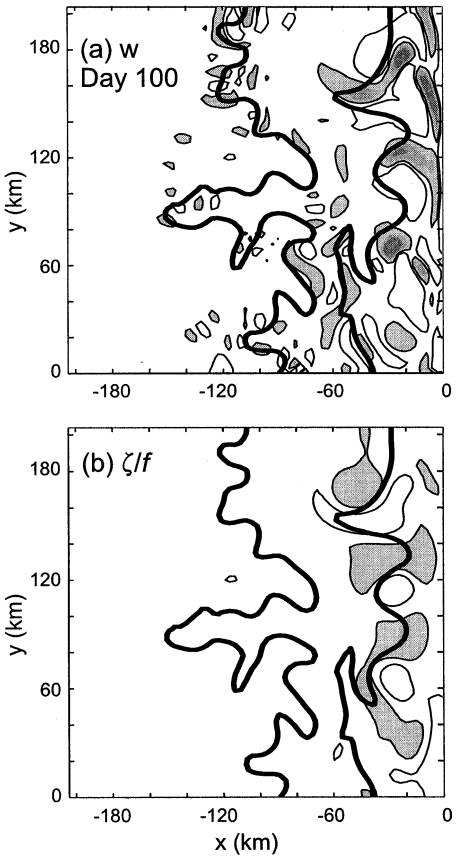

Fig. 7. Contours of (a) vertical velocity at 50 m depth and (b) ζ/f at 30 m depth from the all-inclusive nonhydrostatic solution at day 100. Selected surface isopycnals of $\rho = -0.4$ kg m^{-3} (thick line nearshore) and -0.6 kg m^3 (thick line offshore) are superimposed. Shading indicates downwelling speed in excess of 0.01 cm s^{-1} in (a) and anticyclonic vorticity in excess of $0.2f$ in (b). Contour values are ± 0.01 cm s^{-1} for w and ± 0.2 for ζ/f.

Two measures can be taken to force solutions to approach the hydrostatic limit. One is to remove the vertical Coriolis acceleration from eq. (1) or (2). The other measure is to employ an instantaneous convective adjustment scheme from conventional hydrostatic models to remove

unstable ocean stratification at every time step of integration. For convective adjustment, adjacent cells in a vertical column of sequentially indexed computation cells are paired in two ways: one with an even-numbered box on top and the other with an odd-numbered cell on top. For each type of pairing, the convective adjustment scheme mixes a pair thoroughly if the upper cell is heavier than the lower cell. Since the two-step mixing is done at every time step, it effectively removes all hot spots of unstable stratification. The effect of each measure is briefly discussed below.

In the absence of vertical Coriolis force, Fig. 8 shows the surface density and flow fields (top panel) and vertical velocities at 50 m depth (bottom panel) at day 100. Two surface isopycnals ($\rho = -0.6$ and -0.4 kg m^{-3}) are superimposed in the bottom panel. As in Fig. 7(a), shading indicates downwelling speeds in excess of 0.01 cm s^{-1}. The removal of vertical Coriolis force generally reduces the seaward movement of the meandering front, as indicated by the location of the -0.4 kg m^{-3} contours in Figs. 7(b) and 8(b). Farther offshore, the seaward excursion of the filament as delineated by the -0.6 kg m^{-3} contour is also reduced. In this hydrostatic limit, downwelling occurs preferably under the landward arm of a meander while upwelling is mostly under the seaward arm. A similar conclusion from a reduced-gravity model will be derived later in Section 4. This is the typical behavior as one would expect from a hydrostatic model. The inclusion of vertical Coriolis acceleration is more than enough to reverse this trend [see Fig. 7(a)]. In fact, this drastic change motivated the use of a reduced-gravity model in Section 4 to demonstrate the meander enhancement by the vertical Coriolis force.

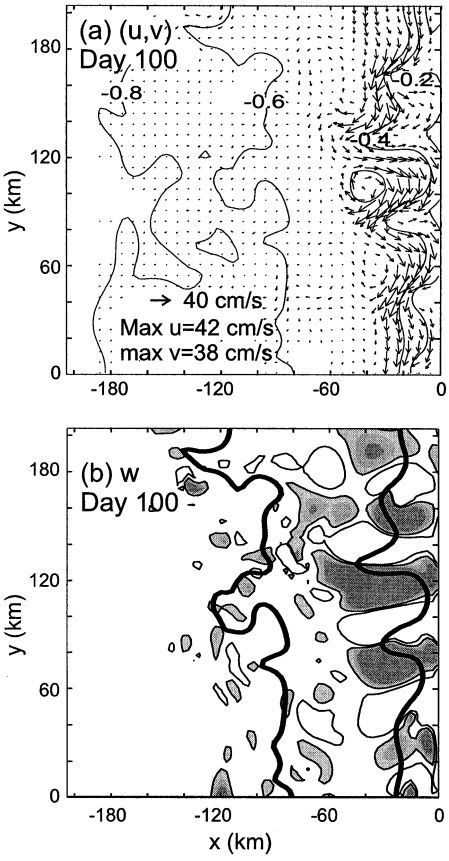

Fig. 8. An illustration of the nonhydrostatic solution in the absence of vertical Coriolis force at day 100: (a) surface flow and the perturbation density field with a contour interval of 0.2 kg m^{-3} and (b) vertical velocity contours of $w = \pm 0.01$ cm s^{-1} at 50 m depth. Surface isopycnals of $\rho = -0.4$ and -0.6 kg m^{-3} (thick lines) are superimposed in (b). Shading indicates downwelling speed in excess of 0.01 cm s^{-1}.

The removal of unstable ocean stratification from the all-inclusive experiment produces much more visible changes. Figure 9 shows solutions at day 100 with the enforcement of the convective adjustment scheme at every time step of integration. As in Fig. 8, the top panel shows surface features, and the bottom panel shows *w*-contours at 50 m depth with the same surface isopycnals superimposed. Seaward movement of the surface front is reduced almost everywhere. Meanders and eddies also have much smaller amplitude, and the otherwise present filament is conspicuously missing. The retardation of the seaward excursion and meander growth by the convective adjustment scheme is conceivable. Seaward intrusion of the dense plume over lighter fluid is shallower near the nose than in the rear due to downward convection. If the convective adjustment scheme is enforced, the nose of intrusion becomes as thick as the rear because of artificial vertical mixing. The smaller density contrast between the intruding plume and the receiving water decreases the intrusion speed. Consequently, the distribution of the vertical velocity in Fig. 9(b) is once again dictated by vertical Coriolis acceleration. Downwelling tends to occur under the seaward arm of a mean-

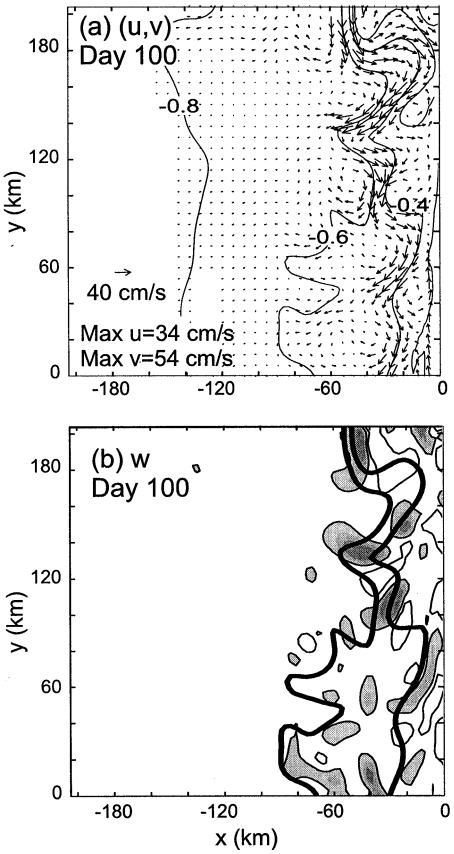

Fig. 9. As in Fig. 8 except the vertical Coriolis force is restored but unstable ocean stratification is removed using a convective adjustment scheme.

der, and upwelling is mostly under the landward segment.

In general, a characteristic vertical flow speed can be used as a measure to indicate the amount of nonhydrostatic contribution to the solution. Among the three solutions shown in this section, the maximum w in the basin is generally the highest in the all-inclusive experiment at any given time. The removal of the vertical Coriolis force reduces the maximum w substantially, but not as much as the reduction caused by the convective adjustment scheme. At day 100, for example, the maximum w in the entire basin is $0.6\ \mathrm{cm\ s^{-1}}$ for the all-inclusive experiment, about $0.3\ \mathrm{cm\ s^{-1}}$ if the vertical Coriolis force is removed, and $0.17\ \mathrm{cm\ s^{-1}}$ with the removal of unstable ocean stratification.

4. Diagnosis of vertical Coriolis force using a reduced-gravity model

The vertical Coriolis force can be incorporated, perhaps somewhat heuristically, into a reduced-gravity model, helping illustrate how it enhances meander growth in the simplest possible setting. For a single layer of the upper ocean bounded below by a density interface, the vertically integrated equations of motion are

$$\frac{\partial \boldsymbol{V}}{\partial t} + (\nabla \cdot \boldsymbol{V} + \boldsymbol{V} \cdot \nabla)\boldsymbol{v} + \boldsymbol{k} \times f\boldsymbol{V} = -g'h\nabla\eta + A\nabla^2\boldsymbol{V} \tag{8}$$

$$\left(\frac{\partial}{\partial t} + \varepsilon\right)\eta + \nabla \cdot \boldsymbol{V} = Q \tag{9}$$

where η is the density interface displacement from a constant depth h_0, $h = h_0 + \eta$ is the upper ocean layer thickness, $\boldsymbol{v}$ is the horizontal velocity vector, $\boldsymbol{V} = h\boldsymbol{v}$ is the depth-integrated current vector, $\boldsymbol{k}$ is a unit vector pointing vertically upward, $f = 2\Omega \sin\phi$ is the constant Coriolis parameter, g' is the reduced gravity characterizing the density interface, and A is the horizontal eddy viscosity. In the continuity equation (9), a positive Q brings water to the upper ocean while a negative Q takes the water away. In light of eq. (1), a sensible choice is to make Q proportional to the zonal velocity u

$$Q = Q_0 h_0 (2\Omega \cos\phi) u / V_0 \tag{10}$$

where Q_0 is a dimensionless constant, $2\Omega \cos\phi$ is brought in to scale down Q, u is positive eastward and negative westward, and V_0 is the velocity characterizing the speed of a meandering jet. In eq. (10), the upper ocean detrains water downward for westward flow but gains water from below for eastward flow. Thus, the addition of Q in eq. (9) essentially incorporates the effect of a nonhydrostatic component, i.e., the vertical Coriolis force, into the reduced-gravity model. The dependence of Q on the zonal velocity makes the reduced-gravity model slightly unstable. For this reason, a small amount of Newtonian damping ($\varepsilon = 0.01\ \mathrm{d^{-1}}$), is introduced to stabilize the computation.

It is important to note that Q acts as forcing in eq. (9) only if the zonal velocity is not zero. Thus, Q is strongest where the initial jet has the largest zonal speed. A steady meridional jet will not be affected by Q. Furthermore, for small-scale disturb-

ances, the zonal speed is small, and Q would be too small to make a difference. Variations of Q in eq. (9) only change the upper layer thickness; this model discounts diapycnic fluid exchange processes that are often included in more sophisticated layer models such as McCreary et al. (1991) and Røed and Shi (1999). This simplification is intended to diagnose the Q-effect in the simplest possible setting.

A meandering jet is initialized following a sinusoidal path

$$x_0' = x_0 + \frac{L_y}{4n} \sin \frac{2\pi n y}{L_y} \tag{11}$$

where x_0 is the mean zonal location of the jet, L_y is the domain length in the meridional direction, n is the wavenumber, and the meander path oscillates about x_0 with an amplitude $L_y/(4n)$. A jet following the meander path is initialized as

$$(u, v) = -V_0 \exp\left(-\frac{(x - x_0')^2}{l^2}\right) \times \frac{\left(\frac{\pi}{2}\cos(2\pi n y/L_y), 1\right)}{1 + \frac{\pi^2}{4}\cos^2(2\pi n y/L_y)} \tag{12}$$

where l is the e-folding width of the jet. The initial interface displacement (η) is computed from eq. (12), assuming the initial jet is geostrophic.

Solutions are derived with a horizontal grid spacing of 3 km. The horizontal domain size is 210 km by 210 km, as in the nonhydrostatic model. The basin is bounded to the east by a straight and free-slip coastline. The western boundary is open; normal gradients of η and $\boldsymbol{v}$ are zero on the open boundary. The coastal ocean is cyclical in the meridional direction. Other parameters are $h_0 = 100$ m, $V_0 = 40$ cm s^{-1}, $n = 4$, $l = 10$ km, $x_0 = -50$ km, $g' = 1$ cm s^{-2}, $A = 10^4$ cm^2 s^{-1}, and $\phi = 40°$N. The choices of the meander wavelength, meander amplitude, and jet speed are guided by the three-dimensional nonhydrostatic solutions presented in Section 3. Other choices would lead to qualitatively similar conclusions and will not be presented. Figure 10 shows the initial jet and interface displacement; shading indicates upward interface displacement in excess of 1 m. The meandering jet is subsequently driven by the source/sink term (Q) alone. If Q is removed, the jet would only be subject to weak dissipation because all parameters controlling dissipation have been adjusted to minima, below which the computation becomes unstable.

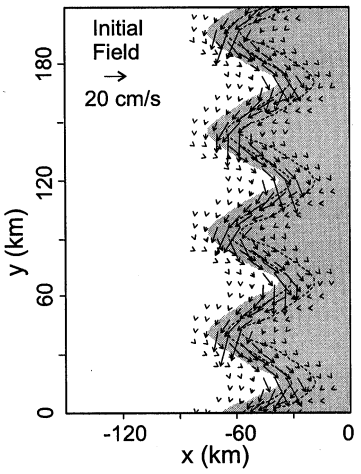

Fig. 10. The initial flow field and interface displacement of a meandering equatorward jet off an eastern ocean boundary at 40°N in the reduced-gravity model. Shading indicates interface elevation in excess of 1 m. Interface elevation contours start from 10 m with an increment of 10 m.

Figure 11 contrasts quasi-linear solutions at day 60 with $Q_0 = 0$ (left panel) and $Q_0 = 0.01$ (right panel). The solutions are quasi-linear in the sense that advection terms are removed from momentum equations; the nonlinear effect arises solely from the cross product of h and $\boldsymbol{v}$ ($\boldsymbol{V} = h\boldsymbol{v}$) in the diffusion term in eq. (8), and the divergence term ($\nabla \cdot \boldsymbol{V}$) in the continuity equation (9). Without forcing, deviation from the initial flow field is slight. With $Q_0 = 0.01$, four changes occur. First, meander crests in the nearshore region begin to tilt in the downstream direction of the jet because seaward flow gains cyclonic rotation tendency while landward flow gains anticyclonic rotation tendency. Second, the seaward current is much stronger than the landward current along a meander. Conceivably, downward detrainment under a seaward current decreases the layer thickness and therefore steepens the interface slope. By virtue of geostrophy, the seaward current is strengthened in this process. On the other hand, upward entrainment under a landward current thickens the upper layer, reduces the interface slope, and weakens the landward current. Third,

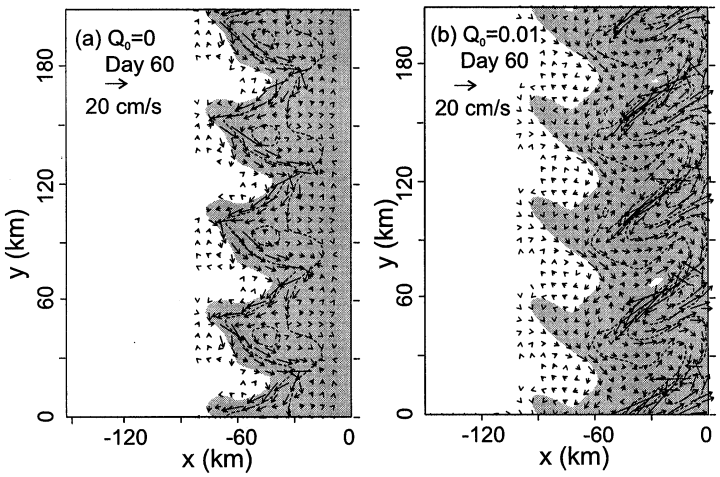

Fig. 11. The quasi-linear solution for a meandering equatorward jet off an eastern ocean boundary at day 60 with (a) $Q_0 = 0$ and (b) $Q_0 = 0.01$. Shading indicates interface elevation above 1 m, and contours start from 10 m with an increment of 10 m.

the dominance of seaward flow over landward flow causes the interface to rise continuously due to a net loss of water by the dominating downward detrainment. The area of the steepest interface moves landward slowly in this quasi-linear system. Consequently, the meander jet shifts landward. Fourth, filaments grow as a result of Q-forcing.

The quasi-linear solutions point out the Q-effect in the simplest possible setting. Along a meandering jet, the seaward portion of the jet must gain a cyclonic rotation tendency continuously in order to complete the U-turn. This tendency is reinforced by Q. The landward portion of the jet also acquires additional anticyclonic rotation tendency from Q. Thus, Q acts as a restoring force for meanders against numerical damping. In this way, meanders may gain strength or at least do not lose strength quickly against dissipative forces. Since a large-amplitude meander is the precursor of a filament, it is quite conceivable that Q also enhances the growth of filaments, however slightly.

Conclusions derived from the reduced-gravity model are merely suggestive, indicating that the vertical Coriolis force enhances the growth of meanders and filaments. Confirmation in the nonhydrostatic regime in Section 3 justifies the heuristic analysis.

5. Discussion and conclusions

With coastal upwelling filaments off eastern ocean boundaries in mind, a nonhydrostatic three-dimensional model is used to evaluate the effect of two mechanisms that emerge in the nonhydrostatic regime. The first mechanism is caused by the projection of Coriolis force in the vertical direction. It is found that this mechanism often enhances meander growth off eastern ocean boundaries. The second mechanism arises from the unstable ocean stratification when cold upwelled water intrudes seaward over the warm layer offshore. Conventional hydrostatic models eliminate this mechanism by enhancing vertical mixing. In the nonhydrostatic regime, unstable stratification is gradually removed in time by downward convection. Although transient, the unstable stratification has the tendency to hasten the growth of meanders and filaments off eastern ocean boundaries. The foregoing conclusions appear to be robust because similar trends persist over a range of horizontal resolutions (from 3 to 10 km) in our preliminary experiments.

The present investigation is highly qualitative in the sense that the two nonhydrostatic mechanisms are examined in models with minimal viscosity and mixing. The purpose is to derive

conclusions that are independent of a particular turbulence closure scheme. Commonly used turbulence closure schemes are normally tuned to fit hydrostatic models. The establishment of widely accepted turbulence closure schemes in the nonhydrostatic regime awaits future development.

Leaving the two nonhydrostatic mechanisms aside, the behavior of large-amplitude meanders and filaments in the nonhydrostatic regime is otherwise similar to that in the hydrostatic regime. For example, upwelling-favorable winds, outcrop of upwelling fronts, β-dispersion, and the use of biharmonic mixing in lieu of conventional Laplacian mixing were all found to enhance the growth of meanders and filaments in our preliminary experiments. Similar conclusions had been obtained earlier using hydrostatic models by McCreary et al. (1991), Batteen (1997) and Røed and Shi (1999). In this light, the present investigation does not change our understanding of how meanders and filaments behave in a local environment. It merely points out that the realism of a model can be enhanced by including nonhydrostatic contributions, insofar as meanders and filaments off eastern ocean boundaries are concerned.

6. Acknowledgments

The authors were supported by the Arctic Sciences Section, Office of Polar Programs of the US National Science Foundation under grants OPP-9709952 (to SYC) and OPP-9614107 (to PTS), respectively. Three anonymous reviewers have contributed significantly to the presentation of this work. This is UMCES contribution Number 3451.

REFERENCES

Batteen, M. L. 1997. Wind-forced modeling studies of currents, meanders, and eddies in the California Current System. *J. Geophys. Res.* **102**, 985–1010.

Brink, K. H. 1987. Coastal ocean physical processes. *Rev. Geophys.* **25**, 204–216.

Bryan, K. 1969. A numerical method for studying the world ocean. *J. Comput. Phys.* **1**, 347–376.

Chao, S.-Y. 1994. Zonal jets over topography on a β-plane, with applications to the Kuroshio Extension over the Shatsky Rise. *J. Phys. Oceanogr.* **24**, 1512–1531.

Davis, R. E. 1985. Drifter observations of coastal surface currents during CODE. The method and descriptive view. *J. Geophys. Res.* **90**, 4741–4755.

Flament, P. L., Armi, L. and Washburn, L. 1985. The evolving structure of an upwelling filament. *J. Geophys. Res.* **90**, 11765–11778.

Fukamachi, Y., McCreary, J. P. and Proehl, J. A. 1995. Instability of density fronts in layer and continuously stratified models. *J. Geophys. Res.* **100**, 2559–2577.

Gill, A. E. and Clarke, A. J. 1974. Wind-induced upwelling, coastal currents, and sea-level changes. *Deep-Sea Res.* **21**, 325–345.

Haidvogel, D. B., Beckmann, A. and Hedstrom, K. S. 1991. Dynamical simulations of filament formation and evolution in the Coastal Transition Zone. *J. Geophys. Res.* **96**, 15 017–15 040.

Haynes, R. E., Barton, E. D. and Pilling, I. 1993. Development, persistence and variability of upwelling filaments off the Atlantic Coast of the Iberian Peninsula. *J. Geophys. Res.* **98**, 22 681–22 692.

Kielmann, J. and Käse, R. H. 1987. Numerical modeling of meander and eddy formation in the Azores Current frontal zone. *J. Phys. Oceanogr.* **17**, 529–541.

Kosro, P. M. and Huyer, A. 1986. CTD and velocity surveys of seaward jets off northern California, July 1981 and 1982. *J. Geophys. Res.* **91**, 7680–7690.

McCreary, J. P. 1981. A linear stratified ocean model of the coastal undercurrent. *Philos. Trans. R. Soc. London* **A302**, 385–413.

McCreary, J. P. and Chao, S.-Y. 1985. Three-dimensional shelf circulation along an eastern ocean boundary. *J. Mar. Res.* **43**, 13–36.

McCreary, J. P., Fukamachi, Y. and Kundu, P. K. 1991. A numerical investigation of jets and eddies near an eastern ocean boundary. *J. Geophys. Res.* **96**, 2515–2534.

Marshall, J., Adcroft, A., Hill, C., Perelman, L. and Heisey, C. 1997. A finite-volume, incompressible Navier–Stokes model for studies of the ocean on parallel computers. *J. Geophys. Res.* **102**, 5753–5766.

Mellor, G. L. 1993. A three-dimensional, primitive equation, numerical ocean model. Atmospheric and Oceanic Sciences Program, Princeton University Technical Report, 35 pp.

Mellor, G. L. and Yamada, T. 1974. A hierarchy of turbulence closure models for planetary boundary layers. *J. Atmos. Sci.* **31**, 1791–1806.

Narimousa, S. and Maxworthy, T. 1989. Application of a laboratory model to the interpretation of satellite and fluid observations of coastal upwelling. *Dyn. Atmos. Oceans* **13**, 1–46.

Pozrikidis, C. 1997. *Introduction to theoretical and computational fluid dynamics*, Oxford University Press, 675 pp.

Røed, L. P. and Shi, X. B. 1999. A numerical study of the dynamics and energetics of cool filaments, jets and

eddies off the Iberian Peninsula. *J. Geophys. Res.* **104**, 29 817–29 841.

Shi, C. and Chao, S.-Y. 1995. Bifurcation of eastward jets induced by mid-ocean ridges and diverging isobaths. *Tellus* **47A**, 1032–1046.

Shi, X. B. and Røed, L. P. 1999. Frontal instabilities in a two-layer, nonisopycnic ocean model, *J. Phys. Oceanogr*. **29**, 948–968.

Sousa, F. M. 1995. Mesoscale processes off the Portuguese coast using satellite and in situ observations (in Portuguese with extended English summary), Ph.D. dissertation, University of Lisbon, Lisbon.

Williams, G. P. 1969. Numerical integration of the three-dimensional Navier–Stokes equations for incompressible flow. *J. Fluid Mech.* **37**, 727–750.